# The rheological response of magma to nanolitisation

Luiz Pereira, Yannick Linard, Fabian B Wadsworth, Jérémie Vasseur, Kai-Uwe Hess, Roberto Moretti, Donald B Dingwell, Daniel R. Neuville

## To cite this version:

Luiz Pereira, Yannick Linard, Fabian B Wadsworth, Jérémie Vasseur, Kai-Uwe Hess, et al.. The rheological response of magma to nanolitisation. Journal of Volcanology and Geothermal Research, 2024, 448 (1), pp.108039. 10.1016/j.jvolgeores.2024.108039 . hal-04665439

HAL Id: hal-04665439
https://hal.science/hal-04665439v1

Submitted on 31 Jul 2024

Journal of Volcanology and Geothermal Research 448 (2024) 108039

Contents lists available at ScienceDirect

Journal of Volcanology and Geothermal Research

journal homepage: www.journals.elsevier.com/journal-of-volcanology-and-geothermal-research

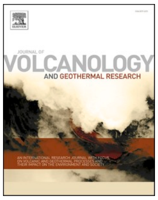

# The rheological response of magma to nanolitisation

Luiz Pereira[a,*], Yannick Linard[b], Fabian B. Wadsworth[c], Jérémie Vasseur[a], Kai-Uwe Hess[a], Roberto Moretti[d], Donald B. Dingwell[a], Daniel R. Neuville[b]

[a] Deepartment of Earth and Environmental Sciences, Ludwig-Maximilians-Universität München, Theresienstr. 41, Munich 80333, Germany
[b] Institut de Physique du Globe de Paris, Université Paris-Cité, 75005 Paris, France
[c] Earth Sciences, Durham University, Durham DH1 3LE, United Kingdom
[d] Department of Engineering, Università degli Studi della Campania "Luigi Vanvitelli", 80131 Aversa (CE), Italy

ARTICLE INFO

*Keywords:*
Nanolites
Magma
Rheology
Nanocrystals
Volcanism

ABSTRACT

Viscosity exerts a fundamental control on magmatic kinetics and dynamics, controlling magma ascent, eruptive style, and the emplacement of lava. Nanolites – crystals smaller than a micron – are thought to affect magma viscosity, but the underlying mechanisms for this remain unclear. Here, we use a cylinder compression creep technique to measure the viscosity of supercooled silicate liquids with different amounts of iron (0–20 wt% $FeO_{tot}$) as a function of temperature, applied shear stress, and time. Sample viscosity was independent on the applied shear stresses, and as expected, melt viscosity decreases as temperature is increased, but only until a critical temperature where a time-dependent increase in viscosity occurs for samples contaning 6.0 wt% $FeO_{tot}$ or more. The magnitude of this increase is controlled by the melt iron content. At constant temperature, these changes are substantial and can reach up to three orders of magnitude for the sample with the most iron. Using transmission electron microscopy, X-ray diffraction, and viscosity modelling, we conclude that this viscosity increase is caused by the formation of nanolites. By using scaling approaches to test suspension effects with and without crystal aggregation, we conclude that the nanolites have only a minimal direct physical effect on the observed viscosity change. Rather, our models show that it is the chemical shift in the groundmass silicate melt composition associated with non-stoichiometric crystallisation that dominates the observed viscosity increase. These findings suggest that iron-rich silicates may encounter chemical viscosity jumps once certain elements are removed from the melt phase to form nanolites. Our work demonstrates an underlying mechanism for the role played by nanolites in viscosity changes of magmas.

## 1. Introduction

The rheology of magmas is of paramount importance in controlling magma ascent and volcanic eruption dynamics (Cassidy et al., 2018; Gonnermann and Manga, 2013). Changes in temperature and water content have a well-understood first-order impact on silicate melt viscosity (Giordano et al., 2008; Hui and Zhang, 2007). However, magmas are not single-phase silicate melts and the physical presence of phases such as crystals and bubbles are known to affect the rheological response of these systems (Costa et al., 2009; Faroughi and Huber, 2023; Frontoni et al., 2022; Mader et al., 2013; Mueller et al., 2010). Constitutive models for the effect of crystals on magma rheology are largely empirical (Caricchi et al., 2007; Costa et al., 2009; Lavallée et al., 2007; Lejeune and Richet, 1995; Pistone et al., 2016) and the underlying mechanistic details of the effect of crystals on magma rheology are still not fully understood. The interactions between crystals and the melts from which they grow may be complex, especially during dynamic crystallisation (Kolzenburg et al., 2016). For example, the widely observed shear-thinning behaviour of crystal-bearing silicates (Caricchi et al., 2007; Lejeune and Richet, 1995) may be attributable to elevated strain rates in the gaps between crystals, leading to local non-Newtonian behaviour in the melt (Vasseur et al., 2023). The viscosity of these multiphase systems can increase by orders of magnitude due to the formation of crystals, bubbles, or droplets of secondary melt (Caricchi et al., 2007; Chevrel et al., 2015; Di Fiore et al., 2022; Frontoni et al., 2022; Lejeune and Richet, 1995; Llewellin and Manga, 2005; Manga et al., 1998; Soldati et al., 2020; Vetere and Holtz, 2020; Vona et al., 2011). Crystal formation generally causes an increase of the final material viscosity (Maron and Pierce, 1956), while droplets and bubbles can cause an increase or decrease of viscosity, which depends on whether or not these non-rigid

---

* Corresponding author.
*E-mail address:* luiz.pereira@min.uni-muenchen.de (L. Pereira).

https://doi.org/10.1016/j.jvolgeores.2024.108039
Received 13 July 2023; Received in revised form 17 December 2023; Accepted 29 February 2024

particles deform (Llewellin and Manga, 2005; Manga et al., 1998; Pereira et al., 2023; Truby et al., 2015). The effects mentioned here are expected to have direct consequences for magma dynamics and eruptive style (Arzilli et al., 2022; Cassidy et al., 2018; Wadsworth et al., 2018).

Nano-crystallisation in magmas was first described some decades ago (Sharp et al., 1996), when the term 'nanolite' was coined to describe crystals that are less than one micron in size. Recent studies have shown different mechanisms by which nanolites can be formed in volcanologically relevant silicates. In a dacitic composition, it has been shown that nanolites were formed in regions that have undergone $H_2O$ degassing (Pistone et al., 2022). More recently, for natural basinites from the 2018–2021 Fani Maoré submarine lavas (Comoros archipelago), nanolites were found to have nucleated inside iron-rich nanodroplets (Thivet et al., 2023). For aluminosilicate compositions, spectroscopic techniques show that nanolites are formed preferentially in regions where there were heterogeneous distribution of cations, i.e., via local segregation of ions (in this case Fe) that favours nucleation (Cormier, 2023). Their formation has been invoked as a key mechanism in eruption dynamics (Cáceres et al., 2021; Cáceres et al., 2020; Di Genova et al., 2020a; Di Genova et al., 2018; Di Genova et al., 2020b; Knafelc et al., 2022; Mujin and Nakamura, 2014; Okumura et al., 2022; Pistone et al., 2022; Scarani et al., 2022; Thivet et al., 2023; Yoshida et al., 2023). Nanolites are thought to have a sufficiently large impact on magma viscosity such that they may induce eruptive style changes from relatively low-hazard effusive eruption styles to relatively high-hazard explosive eruptive styles (Di Genova et al., 2020a). However, the mechanism by which an increase of magma viscosity occurs during nanolite crystallisation remains unclear. In most documented cases, nanolites are composed of Si-poor or Si-free crystals such as magnetite, ilmenite, titanomagnetite, apatite; (Di Genova et al., 2020a; Di Genova et al., 2017; Knafelc et al., 2022; Liebske et al., 2003; Okumura et al., 2022; Scarani et al., 2022; Thivet et al., 2023). The chemical effect in the silicate matrix related to nanolite formation has been reported in the literature in industrially-relevant silicates (Bhattacharyya et al., 2010). An Si-rich and high viscosity halo may initially form around nanolites, similar to the Al-exclusion haloes observed for $TiO_2$ crystals in glass-ceramics (Di Genova et al., 2020b; Zandona et al., 2019). This high-viscosity local zone might affect the viscosity of the whole system. Indeed, the viscosity increase observed during elongation tests on nanolite-bearing andesites was primarily caused by chemical modifications of the silicate matrix (Okumura et al., 2022). In addition to these local compositional changes around nanolites, colloidal forces may act on any small particles (i.e., $<10$ μm), causing them to undergo aggregation (Genovese et al., 2007; Pereira et al., 2022b; Russel, 1980). Such aggregation behaviour can drastically impact the rheological response in crystal-bearing silicates imparting a considerable increase of the viscosity and the appearance of an apparent yield stress (Kurokawa et al., 2022; Machado et al., 2022a). While there is ample evidence for these compositional and aggregation effects in industrially-relevant melts, these effects are not well-investigated in volcanically relevant silicate melts and magmas.

Beyond the effect on viscosity, Fe-rich crystals generally exhibit high gas-solid contact angles with $H_2O$-filled vesicles (Gardner et al., 2022; Shea, 2017). The activation energy for bubble nucleation may be lower and therefore nanolite-bearing magmas may exhibit a higher bubble nucleation rate on decompression (Cáceres et al., 2022; Cáceres et al., 2020; Gardner et al., 2022), because the volatile phases generally wet these crystal phases well. The same high-contact angles can also affect the multiphase dynamics, making outgassing more difficult and may completely change the bubble dynamics of systems (Pereira et al., 2022a; Pereira et al., 2020; Pereira et al., 2023). Clearly then, the identification of nanolites in magmas (Sharp et al., 1996) has a myriad of associated, but largely poorly understood, effects that require careful investigation.

Here, we aim to constrain the effect of nanolites on the viscosity of silicic melts. We use a starting composition that is an iron-free silicic melt, and four other compositions with increasing relative iron content ($FeO_{tot}$: ~2.5, 6, 10 and 20 wt%). We performed viscosity measurements in all samples by varying temperature systematically. For the most volcanological relevant sample (~6.0 wt% $FeO_{tot}$), analyses by transmission electron microscope and X-ray diffraction confirmed the presence of nanolites. We supplement this with calculations to interpret the rheology of this nanolite-bearing sample. In this contribution, by using these experimental results and viscosity modelling, we aim to better understand the effect of nanolite formation on magma rheology.

## 2. Materials and methods

### *2.1. Glass synthesis and compositional analyses*

The starting materials were reagent-grade oxides from Merck® (MgO, CaO, $TiO_2$, $K_2CO_3$, $Na_2CO_3$, $Al_2O_3$, $SiO_2$, and $Fe_3O_4$). Starting materials were dried overnight, and then mixed and ground under ethanol for 1 h in an agate mortar. A starting iron-free silicic composition was chosen and four other compositions with increasing iron content was synthesised by adding iron to this iron-free starting composition. Batches of about 100 g (variability in the exact mass of the batches did not affect the results) were melted in Pt crucibles for 4 h at 1800 K in air, quenched, and reground three times to get a homogeneous glass and then stirred at high temperature to obtain the bubble-free products required for the viscosity measurements. The amorphous nature of the quenched materials before viscosity measurement was checked through optical microscopy and X-ray diffractometry. All glasses were found to be homogeneous before the viscosity measurements. 15 spots on polished sections of each final glass were analysed using a Cameca SX50 electron probe microanalysis (EPMA) under a 15 kV electron acceleration voltage, a current of 10 nA, and 15 s of counting time with a defocused beam. The average composition, molar weight, redox iron ratios (determined by titration; see below), and room-temperature density of each silicic glass is reported in Table 1.

**Table 1**
Chemical composition of studied melts (in wt%) – relative error displayed in parenthesis.[a]

| *Oxides* | *Silicic 1; ~0.0 wt% $FeO_{tot}$* | *Silicic 2; ~2.5 wt% $FeO_{tot}$* | *Silicic 3; ~6.0 wt% $FeO_{tot}$* | *Silicic 4; ~10.0 wt% $FeO_{tot}$* | *Silicic 5; ~20.0 wt% $FeO_{tot}$* |
|---|---|---|---|---|---|
| $SiO_2$ | 62.99 ± 0.13 | 61.75 ± 0.08 | 63.18 ± 0.12 | 55.41 ± 0.12 | 49.56 ± 0.08 |
| $TiO_2$ | 0.60 ± 0.02 | 0.46 ± 0.04 | 0.55 ± 0.04 | 0.48 ± 0.04 | 0.48 ± 0.05 |
| $Al_2O_3$ | 20.64 ± 0.09 | 20.08 ± 0.09 | 20.70 ± 0.11 | 18.04 ± 0.10 | 16.21 ± 0.09 |
| $FeO_{tot}$ | 0.03 ± 0.02 | 2.64 ± 0.09 | 6.79 ± 0.15 | 12.08 ± 0.14 | 21.32 ± 0.15 |
| MgO | 3.27 ± 0.08 | 3.10 ± 0.04 | 3.21 ± 0.04 | 2.87 ± 0.07 | 2.58 ± 0.02 |
| CaO | 8.92 ± 0.12 | 8.30 ± 0.06 | 4.02 ± 0.10 | 7.96 ± 0.11 | 7.06 ± 0.12 |
| $Na_2O$ | 3.55 ± 0.06 | 3.66 ± 0.07 | 1.55 ± 0.06 | 3.15 ± 0.11 | 2.79 ± 0.06 |
| $K_2O$ | 0.95 ± 0.02 | 0.93 ± 0.02 | 0.33 ± 0.03 | 0.82 ± 0.02 | 0.81 ± 0.07 |
| Total | 100.00 | 100.00 | 100.00 | 100.00 | 100.00 |
| $Fe^{2+}/Fe_{tot}$[b] | – | 0.60 | 0.50[d] | 0.64 | 0.58 |
| $Fe^{2+}/Fe_{tot}$[c] | – | | 0.48 | 0.64 | – |

[a] average of 15 EPMA analyses.
[b] obtained via chemical analyses.
[c] obtained via Mossbauer spectroscopy.
[d] obtained via chemical analyses (repeated 14 times).

### 2.2. Iron speciation

Iron speciation, in terms of $Fe^{2+}$, has been constrained via wet-chemical analysis (Neuville et al., 2021; Wilson, 1960). The procedure was to crush ~0.5 g of glass in an agate mortar and transfer it into a Pt-alloy crucible with 7 ml of sulfuric acid, $H_2SO_4$, and 3 ml of hydrofluoric acid, HF. The assembly was then boiled for 3 min and poured into a Pyrex® beaker containing 1 g of boric acid, $H_3BO_3$, 10 ml of $H_2SO_4$, and 5 ml of orthophosphoric acid, $H_3PO_4$. Boric acid neutralises the HF in the solution, while $H_2SO_4$ makes the solution more acidic and so the $H_3PO_4$ forms a complex with iron. Finally, this solution was then dosed by gradual addition of a titrated solution of potassium dichromate, $K_2Cr_2O_7$ (the colour shift of the solution to purple indicates the ferrous iron content). The complete procedure with the involved equations for conversion is described elsewhere (Neuville et al., 2021; Wilson, 1960). The iron speciation in terms of $Fe^{2+}$ is also presented in Table 1.

### 2.3. Total iron content

The total iron content was also obtained via wet-chemical analysis. The idea consists in reducing the iron and determining the total iron in the glass sample using a titrated solution of $K_2Cr_2O_7$. To do so, 1 g of sample was mixed with 40 ml of HF and 5 ml of $H_2SO_4$. The solution was heated until complete evaporation and subsequently 2 g of $H_3BO_3$ and 5 ml of $H_2SO_4$ were added to the remaining material. The new solution was heated again for a few minutes and transferred to a Pyrex® beaker with 500 ml of distilled water. Finally, this last solution was heated up until it becomes totally clear, and at this moment, 50 ml of it is taken away. This latter volume is mixed with 5 ml of $H_2SO_4$, 2 drops of arseniotungstate ($(AsO_4(WO_3H_3)_9)_2$), 2–3 drops of Titanium (III) chloride, $TiCl_3$, until the solution's colour shifts to blue. Potassium dichromate is added until the colour fades, which corresponds to complete oxidisation of $TiCl_3$. 5 ml of acid phosphoric, $H_3PO_4$, was added together with a few drops of barium diphenylamine sulfonate, $C_{24}H_{20}BaN_2O_6S_2$. This last solution is then dosed with potassium dichromate $K_2Cr_2O_7$. The total iron content present in the sample is deduced from the volume of potassium dichromate necessary to observe the colour shift. The complete procedure with the involved equations for conversions is described elsewhere (Neuville et al., 2021; Wilson, 1960).

### 2.4. $^{57}$Fe Mössbauer spectroscopy

The $^{57}$Fe Mössbauer spectra of the quenched glasses were measured to determine the iron oxidation state. Redox ratios were also determined on the same glass samples with Mössbauer spectroscopy carried out at

90 K on 0.2 g powdered samples with a $^{57}$Co source and a standard a-Fe foil for calibration (Mysen et al., 1985). The spectra of reduced samples presented an asymmetric doublet to which we fitted several overlapping Lorentzian elementary doublets. The spectra of the oxidised samples show a symmetric doublet, which was dealt with in the same manner as the $Fe^{2+}$ doublets. The $Fe^{3+}/Fe^{tot}$ ratios were obtained from the relative areas of $Fe^{3+}$ and $Fe^{2+}$ signals. An excellent agreement with the above mentioned wet-chemical analyses was obtained. Table 1 presents the final Fe speciation of the investigated glasses as measured prior to the viscosity measurements at high-temperature.

### 2.5. Viscosity measurements

Viscosity measurements on the supercooled liquids were made in air for different temperatures near the glass transition temperature ($T_g$) interval. These measurements were performed using a high-temperature creep apparatus described elsewhere (Neuville and Richet, 1991). The samples are cylinders of ~5 and ~ 10 mm in diameter and length, respectively. At each temperature, a series of measurements were taken under different applied stresses, which varied in the range between $10^{6.6}$ and $10^{8.9}$ Pa and to verify the Newtonian rheological response of the systems is presented elsewhere (Neuville, 2006). Each viscosity value is the average of 30 measurements made at a given temperature. The standard deviation for these values is always smaller than 0.02 log units. The viscosity measurements were made in a temperature range varying from ~950 until ~1200 K. These experiments were conducted from low to high temperatures. Measurements were taken after ~30 min to allow the thermal equilibration and structural relaxation of the silicate network, in cases of experiments close to glass transition temperature. For measurements above it, relaxation times are much shorter than the experimental time scales. Considering the viscosity of a silicate at its glass transition temperature as $10^{12}$ Pa.s and the infinite frequency shear modulus ($G_\infty$) is ca. $10^{10}$ Pa (Bansal and Doremus, 1986), one can observe through the relaxation time equation ($\tau = (\eta/G_\infty)$), that our experimental time-scale was larger than the relaxation time ($\tau$) of the silicate network at these given temperatures. For some samples, we returned the samples to low temperatures that had already been measured once in order to check for reversibility or hysteretic effects.

### 2.6. Transmission electron microscope (TEM) analyses

Transmission electron microscope analyses on the sample containing ~6.0 wt% of $FeO_{tot}$ after the viscosity measurements (Section 2.5) have been carried out to check the sample nano-scale texture using a Philips CM30 electron microscope operating at 300 kV at the University of Lille (France). Microanalyses were performed either in scanning or nanoprobe mode with a TRACOR energy dispersive spectrometer equipped with a Ge detector. The detector is separated from the TEM column by an ultra-thin window of organic polymer (100 nm thick). This attachment allows the detection of light elements ($Z \geq 5$), especially oxygen. As volatile cations are known to be highly mobile under the electron beam, we used a liquid nitrogen-cooled Be holder for microanalyses. In this case the beam intensities were furthermore reduced to moderate values (electronic density = $10^5$ $Am^{-2}$) by fast scanning over rectangular areas (0.2–0.5 $mm^2$ in size). Several images of the same zone at high magnification ensure that no beam damage could be detected. In order to avoid artefacts due to sample preparation, we simply ground the samples in agate mortar under acetone and we took the powder in suspension.

### 2.7. X-ray diffraction (XRD) and Rietveld refinement

X-ray diffraction was carried out on the sample containing ~6.0 wt% of $FeO_{tot}$ after different heat-treatments' dwell times (0, 330, 570, 1200, and 4800 min) at high temperature (1120 K), in order to reproduce the same temperature-time scenario of the viscosity measurement. X-ray diffraction experiments were performed on a Phillips diffractometer equipped with MoK**α** radiation and a bent graphite monochromator. The intensity measurements were carried out by the q/2q step scanning method and in the angular range $0.5° < 2q < 140°$. The total number of counts accumulated for each measured point was >10,000. The X-ray source was operated at a current of 35 mA and an accelerating voltage of 50 kV. The height, width, and position of the obtained reflections (peaks intensity) were used to determine crystallographic aspects of the observed crystalline phases formed during the above-mentioned heat treatments following the Rietveld technique (Rietveld, 1969) and using the Fullprof program (https://www.ill.eu/sites/fullprof/).

X-ray diffraction is not used routinely as a tool to identify nanolites in magmatic samples because their mass fraction is generally too low to allow quantitative XRD determination (Di Genova et al., 2020a; Di Genova et al., 2018; Di Genova et al., 2020b). Samples with small amounts of crystals (e.g., ~2.0 vol%), XRD was deemed unsuitable for quantitative analysis [e.g., (Schuller et al., 2023)]. However, for samples with a larger crystallinity (here up to 7.5 vol%), quantification using XRD has been successful done (Zandonà et al., 2023b). The major drawback when analysing nanolites using XRD tools is that when the crystallite size decreases to nanoscale dimensions, the XRD peaks broaden (Holder and Schaak, 2019). This effect can be captured using the Scherrer eq. ($D = (\kappa\lambda/\beta \cos\theta)$, which relates the broadening of the peak at a particular diffraction angle ($\theta$) with the crystal size ($D$) and with the width of the peak at half of its height ($\beta$) at the applied X-ray wavelength ($\lambda$). Generally, the Scherrer constant ($\kappa$) is considered to be 0.9, but it may depend on the morphology of the crystal phase (Holder and Schaak, 2019).

## 3. Results

### 3.1. *Rheological response of silicic materials around $T_g$*

The viscosity results for all samples are presented in Fig. 1. These compositions do not show evidence for any change in their viscosities as a function of the applied stress, such that they are Newtonian. The samples Fe-free and containing ~2.5 wt% $FeO_{tot}$ presented a completely reversible behaviour in terms of temperature and applied stress during the viscosity measurements. As one could expect, the sample containing ~2.5 wt% $FeO_{tot}$ is less viscous than the Fe-free sample; this effect of iron has been explained by structural changes experienced by the network (Chevrel et al., 2013; Dingwell and Virgo, 1988; Le Losq et al., 2021a). The viscosity of alumino- and ferro-silicates is inversely correlated to the electronegativity of the trivalent cation and therefore to the ionic characteristic of the $X^{3+}$-$O^{2-}$ bond (where X is either $Al^{3+}$, $Fe^{3+}$ or $Ga^{3+}$; (Dingwell and Virgo, 1988)). The substitution of CaO and MgO by FeO also causes silicate viscosity decrease (Le Losq et al., 2021a). Therefore, both contributions here can explain the decrease in viscosity experienced by the sample containing ~2.5 wt% $FeO_{tot}$ (Fig. 1a).

The samples containing ~6.0 wt% or more of $FeO_{tot}$ display a viscosity that is different from the Fe-free and the 2.5 wt% $FeO_{tot}$ samples described above (Fig. 1b-d). However, as temperature increases (viscosity decreases), the samples containing ~6.0 wt% of $FeO_{tot}$ or more show a viscosity increase at about 1070–1120 K. In that temperature window, the furnace temperature was set constant and the viscosity increase was experimentally monitored over durations of 20 and 60 h until they reached constant equilibrium values. Once stabilised, the temperature was again changed and the viscosity results show another, but elevated, rheological response (Fig. 1b-d). To summarise: we find that samples with high relative iron contents are (1) Newtonian at high temperatures, (2) show a time-dependent increase in viscosity at intermediate temperatures 1070–1120 K until a new, elevated-viscosity equilibrium is reached, and (3) are again Newtonian at low temperatures, albeit on a different, higher viscosity-temperature trend than at high temperatures. Clearly, the time-dependent increase in viscosity in stage (2) represents a shift from one trend of temperature-dependent rheology to another.

### 3.2. *Textural modifications inducing viscosity increase*

To understand the reason for the viscosity increase in the ~6.0 wt% of $FeO_{tot}$ sample, we use TEM and XRD measurements. Using these methods, we observe the presence of nanolites of hercynite spinel ($FeAl_2O_4$) as well as tridymite ($SiO_2$) (Fig. 2 and Fig. 3). Fig. 2 shows a TEM image illustrating the observed hercynite nanolites of ca. 100 nm in size (Feret diameter) with an aspect ratio of about 1. It is important to emphasise that these hercynite nanolites, were formed under oxidising conditions, as previously reported in the literature for Fe—Ti oxide and magnetite nanolites (Cáceres et al., 2021; Yoshida et al., 2023).

To understand the hercynite and tridymite formation in our samples,

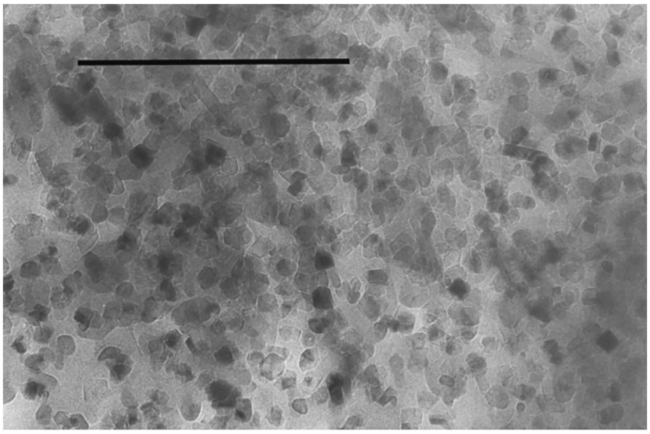

**Fig. 2.** Transmission electron microscope (TEM) image showing a zone rich in hercynite nanolites (dark particles) of about 100 nm and aspect ratio of about 1. The scale bar of the image is equal to 1 μm.

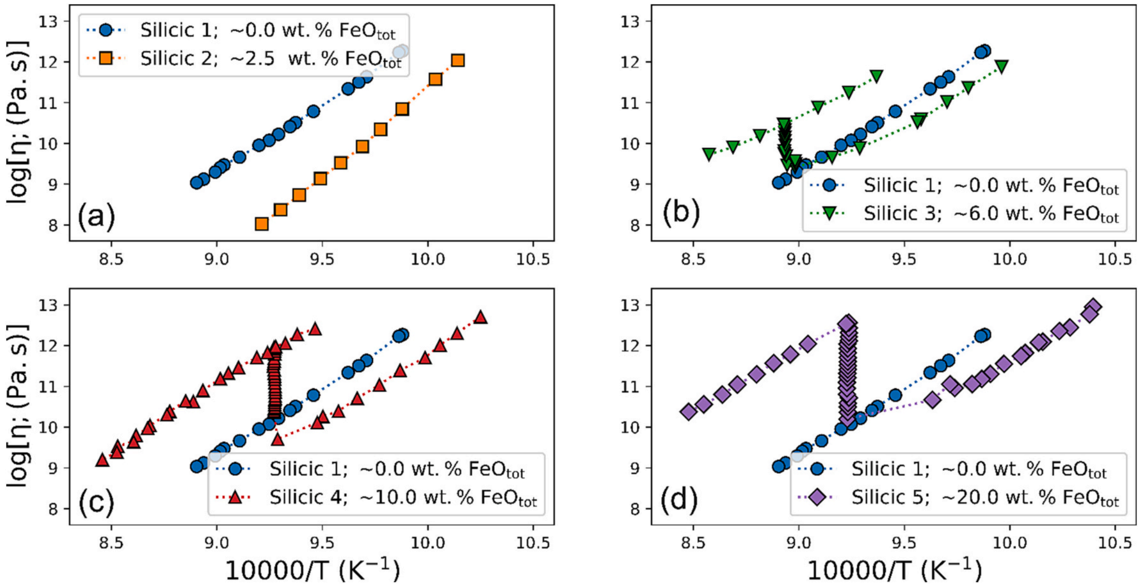

**Fig. 1.** Results of viscometry measurements performed in air using samples containing around 0.0, 2.5, 6.0, 10, and 20 wt% of $FeO_{tot}$ as a function of the reciprocal of temperature. The two Fe-poorest samples show a viscosity decrease with increasing temperature, while the samples containing ~6.0 wt% or more of $FeO_{tot}$ show two stages separated by an increase of viscosity at around 1070–1120 K.

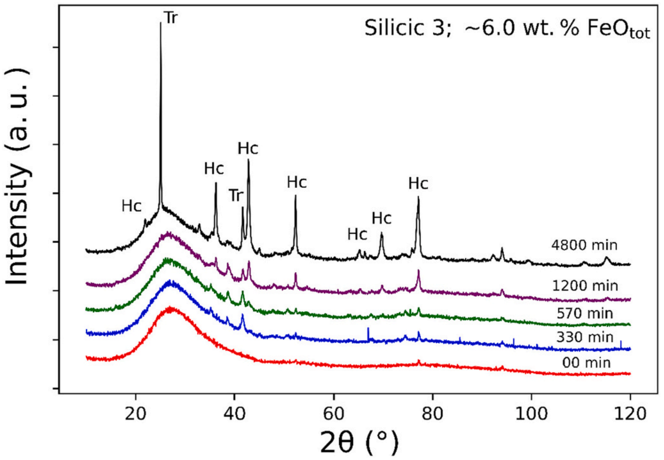

**Fig. 3.** XRD patterns for the sample containing ~6.0 wt% of $FeO_{tot}$ after heat treatments at 1120 K for different durations (labelled). Hercynite and tridymite are abbreviated as Hc and Tr, respectively. The XRD patterns are offset vertically for clarity.

we performed a heat treatment on the sample containing ~6.0 wt% of $FeO_{tot}$ in order to reproduce the same temperature-time conditions in which the viscosity increase from Fig. 1b took place. The results of this heat treatment at 1120 K for several dwell times (0, 330, 570, 1200, and 4800 min) were evaluated via XRD analyses (Fig. 3). X-ray diffraction patterns were analysed using the Fullprof program ($\chi^2 = 4.4$), resulting in the lattice parameter values of 8.173(3) Å for hercynite, and 5.068(3) Å and 8.272 (3) Å for tridymite. The XRD results confirm the presence of hercynite and tridymite. Some pure hercynite [8.153 Å] was added to the final sample, and by a calibration of the intensity of the 311 reflection at 2.45 Å in the X-ray pattern as a function of hercynite added, we could determine the approximate volume percentage of crystals present in our sample (Rietveld, 1969). Therefore, by considering the Rietveld-refined XRD results along with the densities of hercynite and tridymite, we find that the silicic sample containing ~6.0 wt% of $FeO_{tot}$ has 7.5 vol% of each of these phases. These two phases are metastable in this type of silicate system, consistent with previous results (Hill and Roeder, 1974; Schairer and Yagi, 1953).

As discussed in Section 2.7, X-ray diffraction is not routinely used for nanolite detection (see Section 2.7 for the reasons given). In our case, TEM observations provide a 2D estimate of the amount of nanolites in our samples and therefore XRD tests are used in tandem to confirm these estimates. In this study, hercynite nanolites are identifiable by XRD and although their XRD patterns present slightly broader peaks (due to an increase in inelastic scattering typical of nano-sized features); (Holder and Schaak, 2019; Londoño-Restrepo et al., 2019), when compared to tridymite (Fig. 3), this enlargement did not affect the interpretation. XRD analyses are generally precluded for samples containing crystals smaller than the ones analysed here (radius a ~ 50 nm). For example, (Holder and Schaak, 2019; Londoño-Restrepo et al., 2019) showed examples of samples containing crystals of ca. 50 to 25 nm that present already well-defined peak and therefore the ones analysed in this current investigation can be accurately studied using XRD technique.

After the crystallisation stage, the samples returned to a Newtonian rheological response within the applied stress range. It is interesting to notice that the total crystallinity of 15 vol% (hercynite + tridymite), for the sample containing ~6.0 wt% of $FeO_{tot}$, was not enough to make it change from Newtonian to non-Newtonian behaviour (Mueller et al., 2010; Stickel and Powell, 2005). This is similar to previous findings in which pyrope garnet ($Mg_3A1_2Si_3O_{12}$) compositions presenting stoichiometric crystallisation (i.e., crystal composition is the same as that of the parental silicate) remained Newtonian until a crystal fraction of 40 vol% (Lejeune and Richet, 1995).

Considering the initial chemical composition of the sample containing ~6.0 wt% of $FeO_{tot}$ (Table 1) together with a simple stoichiometric calculation (i.e., mass balance) based on the crystallisation of hercynite ($\rho_{hercynite} = 3.95$ g.cm$^{-3}$; crystallinity = 7.5 vol%), we find that almost all iron is consumed during this process. Since the hercynite lattice incorporates iron in its crystallographic structure mainly as $Fe^{2+}$ and the initial sample had a redox ratio of 0.50 ($Fe^{2+}/Fe_{tot}$), a redox reaction must have taken place during the viscosity measurements at temperatures close to $T_g$. Iron redox equilibration at around $T_g$ has been already observed for timescales that are comparable to those of our experiments. For example, on Fe-bearing supercooled $SiO_2$–CaO–MgO–$Na_2O$–FeO liquids at 923 K, equilibration times are of the order of 1000 s (Magnien et al., 2008; Magnien et al., 2006). Most polyvalent elements, including iron, undergo progressive oxidation when temperature decreases towards $T_g$, in agreement with experimental and theoretical observations (Kress and Carmichael, 1991; Le Losq et al., 2020; Moretti, 2005). However, iron oxidation is in contrast with the reduction needed to form hercynite nanolites in our study. At the glass transition temperature range, the redox mechanism consists in the flux of alkali or alkaline-earth cations compensated by a counter-flux of electron holes (i.e., electron transfer from $Fe^{2+}$ to $Fe^{3+}$) that are created by addition of oxygen provided by the oxygen potential gradient to the fluxing cations (Cooper et al., 1996; Le Losq et al., 2021a; Magnien et al., 2008). Therefore, we infer via this mechanism that nanolites form from melt portions depleted by outward migration of fast-diffusing alkali and alkaline-earth ions. This process must have isolated Fe-Al-Si-O melt regions where the expected oxidation did not take place because of the aforementioned crystal formation. Therefore, although iron oxidation in magmas can cause an increase in viscosity (Dingwell and Virgo, 1988), in this specific case due to the reasons given above, we do not consider that this process is responsible for the observed increase in viscosity.

## 4. Discussion

### *4.1. What is the origin of the observed viscosity increase?*

The presence of suspended nanolites in silicate systems may cause viscosity to increase for different reasons, which we test here: (1) classical solid suspension effects arising from crystal drag and interactions [e.g., (Mueller et al., 2010; Stickel and Powell, 2005)]; (2) crystal aggregation effects [e.g., (Di Genova et al., 2020a; Pereira et al., 2022b)], and (3) the change of silicate melt composition and structure during secondary phase formation [e.g., (Pereira et al., 2023; Zandonà et al., 2023a)].

First, we consider classical crystal suspension effects (Mueller et al., 2010; Stickel and Powell, 2005). While there are many rheological laws for the effect of crystals – or any solid particles on the viscosity of a suspension $\eta_s$, a general and useful law for this effect is the Maron-Pierce law (Maron and Pierce, 1956), which is: $\eta_s = \eta(1 - \phi/\phi_m)^{-2}$.Here, $\eta$ is the suspending melt viscosity, $\phi$ is the volume fraction of crystals, and $\phi_m$ is the maximum packing of crystals, in which the suspension becomes 'jammed'. Considering the sample containing ~6.0 wt% of $FeO_{tot}$, if we take the suspending silicate matrix viscosity obtained instants before nanolites formation as $\eta = 2 \times 10^9$ Pa.s (Fig. 1b), the measured range of suspension volume fraction $0.075 < \phi < 0.15$ (Fig. 2), and a general and conservative threshold $\phi_m = 0.585$ for crystals of aspect ratio unity (Boyer et al., 2011), we find that the suspension viscosity should be $2.63 \times 10^9 \leq \eta_s \leq 3.6 \times 10^9$ Pa.s. This range is barely elevated above the melt viscosity $\eta$ and is inconsistent with the observed increase of an order of magnitude or more (Fig. 1). Taking other estimates of the maximum packing, which are generally higher than the value used here, would render the calculated suspension viscosity effect even smaller, and even closer to the suspending melt viscosity. Clearly, the volume fraction of nanolites here is insufficient to explain the observed increase in bulk suspension viscosity by the classical drag theories alone. Therefore, we discount this effect as the major one.

Second, we evaluate the role of crystal aggregation as the main controlling factor to explain the observed viscosity increase of the nanolite-bearing silicic melts. When crystal clusters are formed under flow, silicate liquid is trapped as so-called dead-fluid pockets. The result of dead-fluid pockets in the interstices of small-crystal aggregates is that the apparent volume fraction of non-flowing components (crystals + dead-fluid) is far higher than the volume fraction of the crystals alone (Machado et al., 2022a; Pereira et al., 2022b). If there is sufficient dead-fluid involved (e.g., loose aggregates) then the volume fraction of non-flowing components can be sufficient to cause measurable and even large increases in viscosity (Pereira et al., 2022b). Crystal aggregation of this kind occurs under specific conditions of temperature, viscosity of the surrounding melt phase, particle size, and shear deformation regimes (Pereira et al., 2022b; Quemada, 2006; Russel, 1980). Nanolite aggregation has already been suggested as a relevant mechanism inducing viscosity increases in nanolite-bearing liquids (Di Genova et al., 2020a).

In this current work, to evaluate the aggregational behaviour of nanolites, we apply the modified Péclet number, Pe (Quemada, 2006). This is a dimensionless number defined as the ratio of the diffusion transport timescale over the advection transport timescale (Berli and Quemada, 2000; Mewis and Wagner, 2011; Quemada, 2006; Russel, 1980). In the current case, the diffusion is due to Brownian motion (i.e., thermal diffusion) of the suspended nanolites, while the advection is due to external hydrodynamic forces imposed by the viscometer apparatus. For suspensions of hard particles under Brownian motion, the characteristic timescale of Brownian motion ($\lambda_{\mathrm{Br}-int}$) is equivalent to the diffusion time of a particle over a distance equivalent to its own radius (Berli and Quemada, 2000; Mewis and Wagner, 2011; Quemada, 2006; Russel, 1980):

$$\lambda_{\mathrm{Br}-int} = \frac{6\pi\eta a^3}{k_B T + U}, \tag{1}$$

where a is the suspended crystal radius, $k_B$ is the Boltzmann constant, T is the temperature, U is the interactive potential between the crystals. Similarly, there is also a timescale $\lambda_{\mathrm{hy}}$ associated with the hydrodynamic forces under shear deformation (Berli and Quemada, 2000; Quemada, 2006):

$$\lambda_{\mathrm{hy}} = \dot{\gamma}^{-1}, \tag{2}$$

where $\dot{\gamma}$ is the imposed shear strain rate. Therefore, considering these timescales, the modified Pe number is defined as

$$\mathrm{Pe} = \frac{\lambda_{\mathrm{Br}-int}}{\lambda_{\mathrm{hy}}} = \frac{6\pi\eta a^3}{k_B T + U}\dot{\gamma}. \tag{3}$$

Where at low Pe number scenarios ($\mathrm{Pe} \ll 1$), the diffusional forces due to Brownian motion dominates and the system tends to undergo aggregation, while for high Pe numbers ($\mathrm{Pe} \gg 1$), the opposite takes place and the suspended particles are not able to undergo aggregation (Quemada, 2006). It has been shown that the transition between these two mentioned scenarios takes place at $Pe \approx 1$ (Pereira et al., 2022b; Quemada, 2006).

For these analyses, we consider that η remains constant and equal to the value just before crystallisation on the basis that this should be the melt viscosity in Eq. 3 ($\eta = 2 \times 10^9$ Pa.s). Since $SiO_2$-poor crystal formation results in a silica content increase in the melt and viscosity increase, the considered scenario with constant viscosity represents the best situation for aggregation since clustering at low viscosities is favoured (Pereira et al., 2022b). The temperature is constant and equal to 1120 K for the analysed sample (see Fig. 1b). Due to a lack of experimental data for crystals suspended in silicates, we have scanned values for U around the thermal energy term ($k_B T \approx 1.54 \times 10^{20}$ J). Finally, the shear strain rate was obtained by dividing the minimum applied stress ($\sigma = 10^{6.6}$ Pa) by the viscosity value just before nanolite formation. We chose the minimum applied stress to obtain the minimum shear strain rate, which in turn is the best scenario for crystal aggregation. Therefore, we compute the Péclet number for this system as a function of particle radius for varying interactive potential between particles (Fig. 4). Physically, this last term illustrates different tendencies to aggregate, for which larger values show higher aggregation tendency.

Fig. 4 shows the Péclet number as a function of suspended particle radius for varying interactive potentials U. Systems that undergo aggregation under interparticle interactions generally exhibit a transition between aggregated (i.e., high-viscosity plateau) and non-aggregated scenarios (i.e., low-viscosity plateau) at a critical Péclet number $\mathrm{Pe}_c$ equal to unity. Pe values greater than unity illustrate non-aggregated situations while smaller Pe values are related to scenarios of possible aggregation. Fig. 4 demonstrates that for the studied scenario, the Pe values are above unity regardless of the nanolite radius value and regardless of the interactive potential between the suspended particles. Therefore, for these experimental conditions, the nanolites of hercynite are unlikely to aggregate and the observed viscosity increase in Fig. 1 cannot be explained by crystal aggregation.

It is interesting to notice that in a similar manner, researchers also observed nanolite formation in andesite systems around the same temperature range (Okumura et al., 2022). The formation of these nanolites induced an increase of viscosity, which in turn is much smaller than the ones observed via rheology experiments using analogue materials (Di Genova et al., 2020a). This difference between silicate supercooled liquids and analogue materials is mainly linked to the freedom of movement of nanolites within the matrices as well as their interactive potentials. While nanolites are less mobile in the studied materials at the aforementioned experimental conditions, the nanoparticles in silicone oil do not face the same problem due to the extremely low viscosity of this analogue matrix (Di Genova et al., 2020a). However, it is important to underline that crystal aggregation at dynamic conditions do take place in crystal-bearing silicates (Kurokawa et al., 2022; Machado et al., 2022a; Pereira et al., 2022b). The appearance of yield stresses in magmas due to the breakage of crystal clusters formed at high temperature (~ 1450 K) has also been observed (Kurokawa et al., 2022), and the aggregational behaviour of platinum-group element (PGE) particles as a function of time and applied stress has recently been described (Machado et al., 2022a; Machado et al., 2022b).

Third, we assess the role of compositional modifications of the silicate matrix during nanolite crystallisation. In all naturally occurring cases, nanolites are non-stoichiometrically formed from the silicates (i.e., nanolite composition is different from that of the parental silicate). In fact, nanolites are either Si-poor or Si-free, such as magnetite, ilmenite,

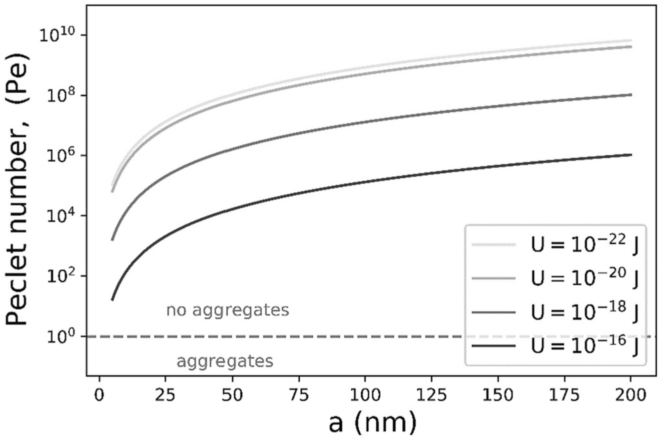

**Fig. 4.** Computation of Péclet number as a function of particle radius for a range of particle interactive potentials U.

titanomagnetite, apatite (Cáceres et al., 2021; Cáceres et al., 2020; Di Genova et al., 2020a; Di Genova et al., 2018; Knafelc et al., 2022; Mujin and Nakamura, 2014; Okumura et al., 2022; Scarani et al., 2022; Thivet et al., 2023). Therefore, during their formation, chemical modifications of the remaining silicate melt take place. To compute these chemical changes in the remaining matrix, we use mass balance to calculate the compositional change for the aforementioned crystallisation step. We depart from the initial sample containing ~6.0 wt% of $FeO_{tot}$ and by stoichiometric subtractions of hercynite ($FeAl_2O_4$, $\rho_{hercynite} = 3.95$ g. cm$^{-3}$, $\phi_{hercynite} \sim 7.5$ vol%) and tridymite ($SiO_2$, $\rho_{tridymite} = 2.3$ g.cm$^{-3}$ $\phi_{tridymite} \sim 7.5$ vol%) until the crystallised volume fraction of each phase is reached. Even though the crystals formed are metastable, as a simplification, we assume here that the system is in equilibrium on the time scale studied. In Fig. 5, we show the calculated chemical evolution of the remaining silicate as a function of the total crystal fraction ($\phi_c = \phi_{hercynite} + \phi_{tridymite}$). Here, for the sake of simplicity, we disregard any elements incorporated in the structure of the crystals formed.

One can observe in Fig. 5 that despite the fact that tridymite crystallisation takes place, globally, the silica content of the remaining matrix still increases during the whole mineral assemblage crystallisation. This behaviour takes place because despite the fact that the melt is getting depleted in $SiO_2$ due to tridymite crystallisation, the total silica molar fraction considering both crystallised minerals (tridymite + hercynite) is much lower ($SiO_2 = 33.3$ mol%) than the initial molar fraction of silica in the sample ($SiO_2 \sim 68$ mol%). Therefore, silica enrichment is expected under the crystallisation of these mentioned phases. An increase in silica induces polymerisation of the silicate network culminating in viscosity increase (Giordano et al., 2008; Russell et al., 2022). Not only experimentally, but also different numerical approaches have shown indirectly a clear viscosity increase during $SiO_2$ enrichment in silicate glasses and melts (Cassar, 2021; Cassar, 2023; Giordano et al., 2008; Hui and Zhang, 2007; Langhammer et al., 2022; Le Losq et al., 2021b).

Besides silica, it is argued that the changes in $Al_2O_3$ content, due to hercynite crystallisation, could cause structural modifications culminating in large viscosity changes (Di Genova et al., 2017). The structure and viscosity of silicate melts are known to be, at first approximation, dependent on the ratio of alkalis, alkaline earth metals, and FeO to $Al_2O_3$ and $Fe_2O_3$. This ratio dictates whether the first one act as network modifiers or charge compensators (Di Genova et al., 2017; Dickenson and Hess, 1982; Mysen and Toplis, 2007). In order to assess the structural impact, we compute the rheological agpaitic index (RAI), calculated on a mol% basis; defined as

$$RAI = \frac{Na_2O + K_2O + CaO + MgO + FeO}{Al_2O_3 + Fe_2O_3}. \tag{4}$$

The denominator of this equation refers to the oxides that require charge balance, while the numerator refers to the oxides that can act either as charge compensator or network modifier. For RAI > 1, on the one hand, there is excess of $Na_2O$, $K_2O$, CaO, MgO, FeO and therefore there exists network modifiers in the structure. For RAI < 1, on the other hand, these mentioned oxides have the role of charge compensators. Here, we compute the RAI at the beginning and at the end of the nanolite formation (Table 2). The obtained values at the beginning and at the end are equal to $RAI_{initial} = 0.89$ and $RAI_{final} = 1.53$, respectively.

These RAI results show that for this particular case of hercynite and tridymite crystallisation from a silicic melt, due to the consumption of alumina during the formation of hercynite, ions which play a charge compensator role become network modifiers, causing the viscosity of the system to decrease (Di Genova et al., 2017; Hess et al., 2001). However, our system shows a clear increase of silica content during the crystallisation stage (Fig. 5) and, therefore, it is expected that polymerisation is enhanced during that process, culminating in viscosity increase. Thus, we have at least two factors that go against one another. While the increase in silica content causes an increase in viscosity, the increase of the RAI parameter causes a decrease in viscosity. It has been shown that in the $SiO_2 - NaAlSi_3O_8 - KAlSi_3O_8$ system that the RAI contribution is more relevant than the $SiO_2$ increase (Hess et al., 2001).

### 4.2. *Viscosity increase of nanolite-bearing silicates*

In Section 4.1, we explored possible explanations for the observed increase in viscosity for the studied Fe-bearing silicic melts. There, we show that the dominant effect is likely to be the change in melt composition arising from non-stoichiometric crystallisation which induces $SiO_2$ increase, rather than bulk suspension effects such as drag and/or aggregation. Knowing the crystal phases and their fractions, in Fig. 5 we show that we can track the evolution of the residual melt composition during crystallisation. Therefore, we can input this evolving composition to the GRD viscosity model (Giordano et al., 2008)

**Table 2**
Chemical composition of studied melts (in wt%) – relative error displayed in parenthesis.

| *Oxides* | *Silicic 3; ~6.0 wt% $FeO_{tot}$ initial* | *Silicic 3; ~6.0 wt% $FeO_{tot}$ final* |
|---|---|---|
| $SiO_2$ | 63.18 | 71.76 |
| $TiO_2$ | 0.55 | 0.68 |
| $Al_2O_3$ | 20.70 | 15.22 |
| $FeO_{tot}$ | 6.79 | 1.12 |
| MgO | 3.21 | 3.95 |
| CaO | 4.02 | 4.96 |
| $Na_2O$ | 1.55 | 1.90 |
| $K_2O$ | 0.33 | 0.41 |
| Total | 100 | 100 |

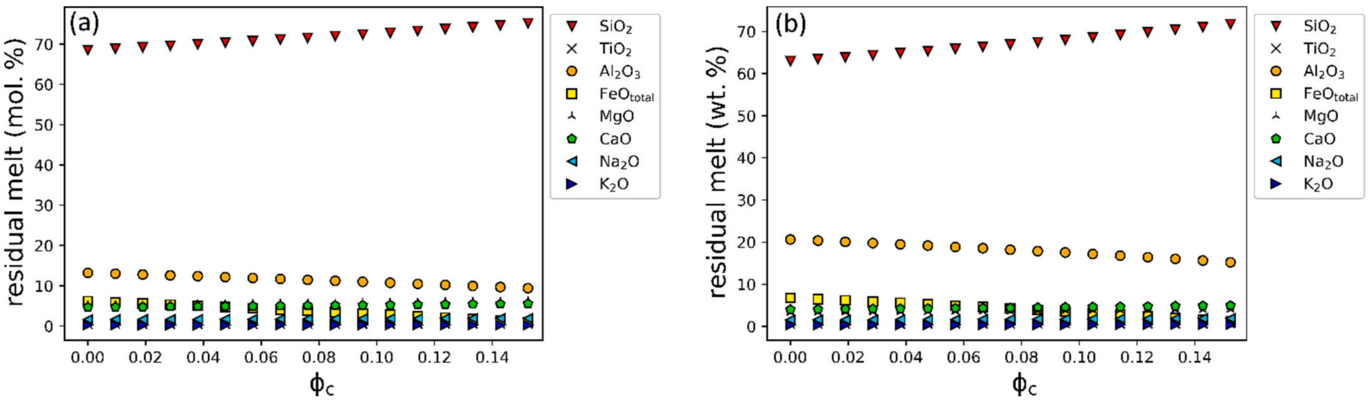

**Fig. 5.** Chemical evolution of the remaining silicate matrix in mol% (a) and in wt% (b) as a function of the total crystal fraction (hercynite + tridymite) during crystallisation obtained via stoichiometric removal of the mentioned phases. The initial and final silicate compositions are displayed in Table 2.

to turn the composition evolution to a calculated viscosity evolution at a given temperature, or as a function of temperature. This calculation gives us the parameter $\eta$ (i.e., the silicate melt viscosity). Returning to the calculation of the suspension viscosity $\eta_s$, we can then compute the viscosity change associated with studied crystallised phases. By accounting for the stoichiometric subtractions of hercynite ($FeAl_2O_4$, $\rho_{hercynite}=$ 3.95 g.cm$^{-3}$, $\phi_{hercynite} \sim 7.5$ vol%) and tridymite ($SiO_2$, $\rho_{tridymite}=$ 2.3 g.cm$^{-3}$ $\phi_{tridymite} \sim 7.5$ vol%) from the initial sample composition containing ~6.0 wt% of $FeO_{tot}$, the suspension viscosity can be calculated for a succession of crystallisation steps. Fig. 6a displays a total alkali vs. silica (TAS) diagram showing the chemical evolution undergone by the silicic melt during crystallisation. The starting andesitic melt (at the interface with dacite field) experiences a $SiO_2$ increase, getting closer to the rhyolite field after the last crystallisation step. Contrastingly, the total alkali content barely increases in the course of crystallisation. Fig. 6b shows the experimentally obtained viscosity results for the sample containing ~6.0 wt% of $FeO_{tot}$ before and after the crystallisation steps (similarly to Fig. 1b). For the sake of comparison, the Fe-free silicic sample is also displayed in this figure (similarly to Fig. 1b). Importantly, we show that the computed trend of $\eta(T)$ and the computed trend of $\eta_s(T)$ are in good agreement with the data after the sharp increase in viscosity associated with crystallisation of nanolites.

In Fig. 6b, that GRD viscosity model does estimate well the viscosity of the sample containing ~6.0 wt% of $FeO_{tot}$ before crystallisation (yellow dotted line). It can be also clearly seen in Fig. 6b that the chemical and structural modifications on the silicate matrix induced by formation of the crystals can explain the viscosity evolution of the crystal-bearing silicate during the crystallisation events. The dotted red line in Fig. 6b shows the pure silicate viscosity of the modified silicate melt after non-stoichiometric extraction of the oxides that formed the formed crystals. By accounting for the small additional physical contribution of the crystals via suspension effects, the calculations estimate well the experimental viscosity values (see dashed red line in Fig. 6b). These results confirm, for this high-viscosity nanolite formation region, that the increase of viscosity is indeed significant and relevant, but it is primarily controlled by the enrichment of the silicate supercooled liquid in $SiO_2$, which in turn confers a viscosity increase. It is important to stress that after the stoichiometric extraction of the oxides that formed the crystals, the final silicate matrix is nearly Fe-free and therefore, the problems observed for estimating the melt viscosity using GRD model is not applicable here (Valdivia et al., 2023). Indeed the iron-bearing viscosity pre-crystallisation is also well matched by the GRD model (Fig. 6b, yellow dotted line). Chemical changes upon Fe-oxide nanolite formation have been recently reported in the literature (Kennedy et al., 2022). They have shown that Fe-oxide nanolite formation influences the distribution of elements in the vicinities of the formed nanolites. For instance, it has been observed a decrease of large cations (i.e., $Ca^{2+}$, $Na^{+}$, $K^{+}$) near the nanolites and a decrease of the average bond length as well, which characterises a strong silicate network nearby these newly formed crystals (Kennedy et al., 2022).

### 4.3. Implications of nanolites for volcanic eruptions

Here, we combine the results obtained in this study together with other results from the literature and discuss the implications of nanolites for the eruptive style of volcanoes. In the present study, the formation of nanolites was observed in a temperature range close to the glass transition temperature. In a similar temperature range, experiments were performed at atmospheric and elevated pressures (100–300 MPa), and a viscosity increase was observed (Liebske et al., 2003). In their case, Liebske et al. (2003) found that the viscosity increase was linked to the appearance of Fe-bearing nanolites with size of order $10-100$ nm. For both Liebske et al. (2003) and the present study, the appearance of nanolites occurred at lower temperatures relative to eruptive temperatures of systems with similar $SiO_2$ content (Nandedkar et al., 2014), indicating that the nanolite formation in these studied case might be a post-eruptive phenomenon on cooling, or associated with cooling during the last portion of ascent. Therefore, it might have direct effects on lava or dome formation and on the last gasp of magma ascent near-surface. The appearance of nanolites near the glass transition temperature range is not surprising. It is already known in the glass community that nano-glass-ceramics are produced in this same temperature range. This is because in this temperature range nucleation rates are elevated while growth rates are relatively small, producing therefore nano-crystals (Jiusti et al., 2020; Montazerian and Zanotto, 2022; Nascimento et al., 2011).

Further, it must be noted that the viscosity increase observed in this current work linked to the physical presence of nanolites (difference between dashed and dotted lines in Fig. 6) is much lower than the observed for nanolite-bearing systems using analogues experiments (Di Genova et al., 2020a). Similarly, elongation viscosity measurements have also led to the conclusion that nanolite-bearing silicates present viscosity increase due to a physical suspension effect, but that the degree of increase is much lower than the one obtained via analogue materials

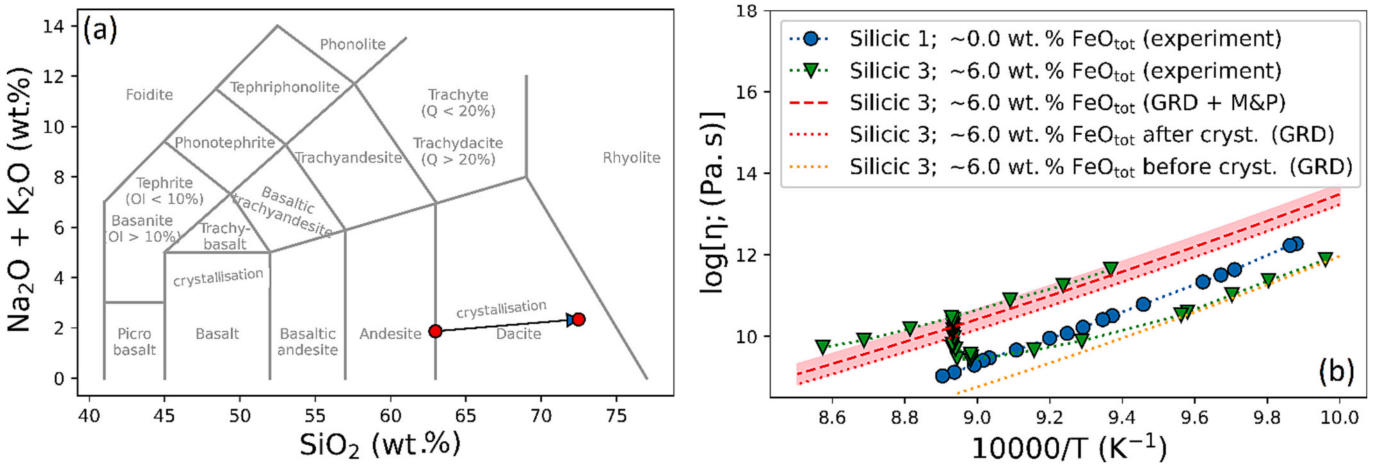

**Fig. 6.** (a) TAS diagram showing the chemical changes undergone by the sample containing ~6.0 wt% of $FeO_{tot}$ during the formation of ~7.5 vol% of hercynite and ~ 7.5 vol% of tridymite and (b) the experimental viscosity results of the Fe-free sample and the sample containing ~6.0 wt% of $FeO_{tot}$ along with modelled viscosity results obtained using GRD model (Giordano et al., 2008) (for the sample containing ~6.0 wt% of $FeO_{tot}$ before and after crystallisation events, dotted lines) and the same model coupled with the Maron and Pierce (1956) model (dashed red line labelled as M&P). The pink region in (b) refers to the error associated with the GRD model (0.25 log units). (For interpretation of the references to colour in this figure legend, the reader is referred to the web version of this article.)

(Di Genova et al., 2020a; Okumura et al., 2022). The liquid viscosity chosen for the analogue tests was 0.136 Pa.s, which is much lower than any observed silicate melt viscosity at eruptive conditions and makes Brownian and/or aggregation effects more likely to happen [see (Pereira et al., 2022b; Quemada, 2006)]. Such Brownian or aggregation effects are less likely to be relevant at magmatic conditions of typical shear strain rates for which the hydrodynamics outweigh the Brownian or attractive dynamics. Therefore, at the conditions of magma emplacement in the crust or on the surface during eruption, we suggest that groundmass chemical changes drive the nanolite-induced viscosity increase.

## 5. Conclusions

We studied the rheological response of silicate systems containing different amounts of iron oxide. We observed that a large viscosity increase takes place for samples containing 6.0 wt% or more of $FeO_{tot}$ during heating. By combining TEM observations and Rietveld-refined XRD analyses, we could attribute this viscosity increase to the presence of nanolites of hercynite spinel ($FeAl_2O_4$) as well as tridymite ($SiO_2$). We critically review the possible mechanisms of viscosity increase associated with the crystallisation. Our analysis shows that hydrodynamic drag and aggregation are not dominant and cannot explain the large viscosity increase in this case owing to the low mobility of the silicate matrix. However, the silica content considerably increases during the crystallisation events and using the GRD model (Giordano et al., 2008) to compute the silicate liquid viscosity along with suspension effects using Maron & Pierce (Maron and Pierce, 1956), we suggest that the viscosity increase is controlled by chemical modifications of the remaining silicate due to the crystallisation of the mentioned phases. We also discuss the implications of nanolite formation and viscosity increase to volcanic eruptions. Due to the temperature range in which these nanolites were formed ($\sim$ 1100 K), this type of crystallisation and consequent the related viscosity increase are likely to be important during subaerial magma emplacement in lavas and domes, and/or during the final stages of magma ascent near the Earth's surface.

## CRediT authorship contribution statement

**Luiz Pereira:** Conceptualization, Data curation, Formal analysis, Funding acquisition, Software, Writing – original draft. **Yannick Linard:** Conceptualization, Data curation, Formal analysis, Investigation, Methodology, Writing – review & editing. **Fabian B. Wadsworth:** Data curation, Formal analysis, Supervision, Validation, Visualization, Writing – review & editing. **Jérémie Vasseur:** Data curation, Formal analysis, Software, Writing – review & editing. **Kai-Uwe Hess:** Formal analysis, Supervision, Validation, Writing – review & editing. **Roberto Moretti:** Formal analysis, Validation, Visualization, Writing – review & editing. **Donald B. Dingwell:** Formal analysis, Funding acquisition, Supervision, Validation, Visualization, Writing – review & editing. **Daniel R. Neuville:** Conceptualization, Data curation, Formal analysis, Investigation, Methodology, Supervision, Visualization, Writing – review & editing.

## Declaration of competing interest

The authors whose names are listed immediately below certify that they have NO affiliations with or involvement in any organization or entity with any financial interest (such as honoraria; educational grants; participation in speakers' bureaus; membership, employment, consultancies, stock ownership, or other equity interest; and expert testimony or patent-licensing arrangements), or non-financial interest (such as personal or professional relationships, affiliations, knowledge or beliefs) in the subject matter or materials discussed in this manuscript.

## Data availability

Data will be made available on request.

## Acknowledgments

Luiz Pereira is grateful for the support of the Alexander von Humboldt Foundation. We acknowledge support of the European Research Council (ERC) 2018 ADV Grant 834225 (EAVESDROP). We also would like to thank Ben Ellis, Mattia Pistone, and an anonymous reviewer for the comments and advice given on the final manuscript version.

## References

Arzilli, F., et al., 2022. Dendritic crystallization in hydrous basaltic magmas controls magma mobility within the Earth's crust. Nat. Commun. 13 (1), 3354.
Bansal, N.P., Doremus, R.H., 1986. Handbook of Glass Properties, New York.
Berli, C., Quemada, D., 2000. Rheological modeling of microgel suspensions involving solid−liquid transition. Langmuir 16.
Bhattacharyya, S., et al., 2010. Direct evidence of Al-Rich Layers around Nanosized ZrTiO4 in Glass: putting the Role of Nucleation Agents in Perspective. Cryst. Growth Des. 10 (1), 379–385.
Boyer, F., Guazzelli, É., Pouliquen, O., 2011. Unifying Suspension and Granular Rheology. Phys. Rev. Lett. 107 (18), 188301.
Cáceres, F., et al., 2020. Can nanolites enhance eruption explosivity? Geology 48.
Cáceres, F., et al., 2021. From melt to crystals: the effects of cooling on FeTi oxide nanolites crystallisation and melt polymerisation at oxidising conditions. Chem. Geol. 563, 120057.
Cáceres, F., et al., 2022. The roles of microlites and phenocrysts during degassing of silicic magma. Earth Planet. Sci. Lett. 577, 117264.
Caricchi, L., et al., 2007. Non-Newtonian rheology of crystal-bearing magmas and implications for magma ascent dynamics. Earth Planet. Sci. Lett. 264 (3), 402–419.
Cassar, D.R., 2021. ViscNet: Neural network for predicting the fragility index and the temperature-dependency of viscosity. Acta Mater. 206, 116602.
Cassar, D.R., 2023. GlassNet: A Multitask Deep Neural Network for Predicting Many Glass Properties. Ceramics International.
Cassidy, M., Manga, M., Cashman, K., Bachmann, O., 2018. Controls on explosive-effusive volcanic eruption styles. Nat. Commun. 9 (1), 2839.
Chevrel, M.O., Giordano, D., Potuzak, M., Courtial, P., Dingwell, D.B., 2013. Physical properties of CaAl2Si2O8–CaMgSi2O6–FeO–Fe2O3 melts: Analogues for extra-terrestrial basalt. Chem. Geol. 346, 93–105.
Chevrel, M., et al., 2015. Viscosity Measurements of Crystallizing Andesite from Tungurahua Volcano (Ecuador). Geochemistry, Geophysics, Geosystems, p. 16.
Cooper, R.F., Fanselow, J.B., Poker, D.B., 1996. The mechanism of oxidation of a basaltic glass: Chemical diffusion of network-modifying cations. Geochim. Cosmochim. Acta 60 (17), 3253–3265.
Cormier, L., 2023. From nanoscale heterogeneities to nanolites: cation clustering in glasses. C. R. Phys. 24, 1–15.
Costa, A., Caricchi, L., Bagdassarov, N., 2009. A model for the rheology of particle-bearing suspensions and partially molten rocks. Geochem. Geophys. Geosyst. 10 (3).
Di Fiore, F., Vona, A., Costa, A., Mollo, S., Romano, C., 2022. Quantifying the influence of cooling and shear rate on the disequilibrium rheology of a trachybasaltic melt from Mt. Etna. Earth Planet. Sci. Lett. 594, 117725.
Di Genova, D., et al., 2017. A compositional tipping point governing the mobilization and eruption style of rhyolitic magma. Nature 552 (7684), 235–238.
Di Genova, D., Caracciolo, A., Kolzenburg, S., 2018. Measuring the degree of "nanotilization" of volcanic glasses: Understanding syn-eruptive processes recorded in melt inclusions. Lithos 318-319, 209–218.
Di Genova, D., et al., 2020a. In situ observation of nanolite growth in volcanic melt: a driving force for explosive eruptions. Sci. Adv. 6, 1–13.
Di Genova, D., Zandona, A., Deubener, J., 2020b. Unravelling the effect of nano-heterogeneity on the viscosity of silicate melts: Implications for glass manufacturing and volcanic eruptions. J. Non-Cryst. Solids 545, 120248.
Dickenson, M.P., Hess, P.C., 1982. Redox equilibria and the structural role of iron in alumino-silicate melts. Contrib. Mineral. Petrol. 78 (3), 352–357.
Dingwell, D.B., Virgo, D., 1988. Viscosities of melts in the Na2O FeO Fe2O3 SiO2 system and factors controlling relative viscosities of fully polymerized silicate melts. Geochim. Cosmochim. Acta 52 (2), 395–403.
Faroughi, S.A., Huber, C., 2023. Rheological state variables: a framework for viscosity parametrization in crystal-rich magmas. J. Volcanol. Geotherm. Res. 440, 107856.
Frontoni, A., Costa, A., Vona, A., Romano, C., 2022. A comprehensive database of crystal-bearing magmas for the calibration of a rheological model. Sci. Data 9 (1), 247.
Gardner, J., et al., 2022. Bubble Formation in Magma. Annu. Rev. Earth Planet. Sci. 51.
Genovese, D.B., Lozano, J.E., Rao, M.A., 2007. The rheology of colloidal and noncolloidal food dispersions. J. Food Sci. 72 (2), R11–R20.
Giordano, D., Russell, J.K., Dingwell, D.B., 2008. Viscosity of magmatic liquids: a model. Earth Planet. Sci. Lett. 271 (1), 123–134.
Gonnermann, H.M., Manga, M., 2013. Dynamics of magma ascent in the volcanic conduit. In: Lopes, R.M.C., Fagents, S.A., Gregg, T.K.P. (Eds.), Modeling Volcanic Processes: The Physics and Mathematics of Volcanism. Cambridge University Press, Cambridge, pp. 55–84.

Hess, K.U., Dingwell, D.B., Gennaro, C., Mincione, V., 2001. Viscosity–temperature behaviour of dry melts in the Qz–Ab–Or system. Chem. Geol. 174 (1), 133–142.

Hill, R., Roeder, P., 1974. The Crystallization of Spinel from Basaltic Liquid as a Function of Oxygen Fugacity. J. Geol. 82 (6), 709–729.

Holder, C.F., Schaak, R.E., 2019. Tutorial on powder X-ray diffraction for characterizing nanoscale materials. ACS Nano 13 (7), 7359–7365.

Hui, H., Zhang, Y., 2007. Toward a general viscosity equation for natural anhydrous and hydrous silicate melts. Geochim. Cosmochim. Acta 71 (2), 403–416.

Jiusti, J., Zanotto, E.D., Cassar, D.R., Andreeta, M.R.B., 2020. Viscosity and liquidus-based predictor of glass-forming ability of oxide glasses. J. Am. Ceram. Soc. 103 (2), 921–932.

Kennedy, E., Sari, B., Scott, M.C., 2022. Chemical and Structural Alterations in the Amorphous Structure of Obsidian due to Nanolites. Microsc. Microanal. 28 (2), 289–295.

Knafelc, J., et al., 2022. Havre 2012 pink pumice is evidence of a short-lived, deep-sea, magnetite nanolite-driven explosive eruption. Commun. Earth Environ. 3 (1), 19.

Kolzenburg, S., Giordano, D., Cimarelli, C., Dingwell, D.B., 2016. In situ thermal characterization of cooling/crystallizing lavas during rheology measurements and implications for lava flow emplacement. Geochim. Cosmochim. Acta 195, 244–258.

Kress, V.C., Carmichael, I.S.E., 1991. The compressibility of silicate liquids containing Fe2O3 and the effect of composition, temperature, oxygen fugacity and pressure on their redox states. Contrib. Mineral. Petrol. 108 (1), 82–92.

Kurokawa, A.K., Miwa, T., Ishibashi, H., 2022. Aging in magma rheology. Sci. Rep. 12 (1), 10015.

Langhammer, D., Di Genova, D., Steinle-Neumann, G., 2022. Modeling Viscosity of Volcanic Melts with Artificial Neural Networks. Geochem. Geophys. Geosyst. 23 (12), e2022GC010673.

Lavallée, Y., Hess, K.-U., Cordonnier, B., Dingwell, D., 2007. A Non-Newtonian Rheological Law for Highly Crystalline Dome Laws. Geology 35, 843–846.

Le Losq, C., Moretti, R., Oppenheimer, C., Baudelet, F., Neuville, D.R., 2020. In situ XANES study of the influence of varying temperature and oxygen fugacity on iron oxidation state and coordination in a phonolitic melt. Contrib. Mineral. Petrol. 175 (7), 64.

Le Losq, C., Cicconi, M.R., Neuville, D.R., 2021a. Iron in Silicate Glasses and Melts. Magma Redox Geochem. 233–253.

Le Losq, C., Valentine, A.P., Mysen, B.O., Neuville, D.R., 2021b. Structure and properties of alkali aluminosilicate glasses and melts: Insights from deep learning. Geochim. Cosmochim. Acta 314, 27–54.

Lejeune, A.-M., Richet, P., 1995. Rheology of crystal-bearing silicate melts: an experimental study at high viscosities. J. Geophys. Res. Solid Earth 100 (B3), 4215–4229.

Liebske, C., Behrens, H., Holtz, F., Lange, R.A., 2003. The influence of pressure and composition on the viscosity of andesitic melts. Geochim. Cosmochim. Acta 67 (3), 473–485.

Llewellin, E.W., Manga, M., 2005. Bubble suspension rheology and implications for conduit flow. J. Volcanol. Geotherm. Res. 143 (1), 205–217.

Londoño-Restrepo, S.M., Jeronimo-Cruz, R., Millán-Malo, B.M., Rivera-Muñoz, E.M., Rodriguez-García, M.E., 2019. Effect of the Nano Crystal size on the X-ray Diffraction patterns of Biogenic Hydroxyapatite from Human, Bovine, and Porcine Bones. Sci. Rep. 9 (1), 5915.

Machado, N., Pereira, L., Neyret, M., Lemaître, C., Marchal, P., 2022a. Influence of platinum Group Metal particle aggregation on the rheological behavior of a glass melt. J. Nucl. Mater. 153618.

Machado, N.M.P., Neyret, M., Lemaître, C., Marchal, P., 2022b. Thixotropic behavior of a glass melt of nuclear interest containing platinum group metal particles. Rheol. Acta 61 (11), 857–866.

Mader, H., Llewellin, E., Mueller, S., 2013. The rheology of two-phase magmas: a review and analysis. J. Volcanol. Geotherm. Res. 257, 135–158.

Magnien, V., et al., 2006. Kinetics of iron redox reactions in silicate liquids: a high-temperature X-ray absorption and Raman spectroscopy study. J. Nucl. Mater. 352 (1), 190–195.

Magnien, V., et al., 2008. Kinetics and mechanisms of iron redox reactions in silicate melts: the effects of temperature and alkali cations. Geochim. Cosmochim. Acta 72 (8), 2157–2168.

Manga, M., Castro, J., Cashman, K.V., Loewenberg, M., 1998. Rheology of bubble-bearing magmas. J. Volcanol. Geotherm. Res. 87 (1), 15–28.

Maron, S.H., Pierce, P.E., 1956. Application of ree-eyring generalized flow theory to suspensions of spherical particles. J. Colloid Sci. 11 (1), 80–95.

Mewis, J., Wagner, N., 2011. Colloidal Suspension Rheology.

Montazerian, M., Zanotto, E., 2022. Nucleation, growth, and crystallization in oxide glass-formers. A current perspective. In: Neuville, D.R., Henderson, G.S., Dingwell, D.B. (Eds.), Reviews in Mineralogy and Geochemistry, pp. 405–429.

Moretti, R., 2005. Polymerisation, basicity, oxidation state and their role in ionic modelling of silicate melts. Ann. Geophys. 48.

Mueller, S., Llewellin, E.W., Mader, H.M., 2010. The rheology of suspensions of solid particles. Proc. Royal Soc. Math. Phys. Eng. Sci. 466 (2116), 1201–1228.

Mujin, M., Nakamura, M., 2014. A nanolite record of eruption style transition. Geology 42 (7), 611–614.

Mysen, B.O., Toplis, M.J., 2007. Structural behavior of Al3+ in peralkaline, metaluminous, and peraluminous silicate melts and glasses at ambient pressure. Am. Mineral. 92 (5–6), 933–946.

Mysen, B.O., Carmichael, I.S.E., Virgo, D., 1985. A comparison of iron redox ratios in silicate glasses determined by wet-chemical and 57Fe Mössbauer resonant absorption methods. Contrib. Mineral. Petrol. 90 (2), 101–106.

Nandedkar, R.H., Ulmer, P., Müntener, O., 2014. Fractional crystallization of primitive, hydrous arc magmas: an experimental study at 0.7 GPa. Contrib. Mineral. Petrol. 167 (6), 1015.

Nascimento, M.L.F., Fokin, V.M., Zanotto, E.D., Abyzov, A.S., 2011. Dynamic processes in a silicate liquid from above melting to below the glass transition. J. Chem. Phys. 135 (19).

Neuville, D.R., 2006. Viscosity, structure and mixing in (Ca, Na) silicate melts. Chem. Geol. 229 (1), 28–41.

Neuville, D.R., Richet, P., 1991. Viscosity and mixing in molten (Ca, Mg) pyroxenes and garnets. Geochim. Cosmochim. Acta 55 (4), 1011–1019.

Neuville, D.R., Cicconi, M.R., Le Losq, C., 2021. How to measure the Oxidation State of Multivalent elements in Minerals, Glasses, and Melts? Magma Redox Geochem. 255–281.

Okumura, S., et al., 2022. Rheology of nanocrystal-bearing andesite magma and its roles in explosive volcanism. Commun. Earth Environ. 3 (1), 241.

Pereira, L., et al., 2023. Rheology of a sodium-molybdenum borosilicate melt undergoing phase separation. Int. J. Appl. Glas. Sci. 1–12.

Pereira, L., Podda, O., Fayard, B., Laplace, A., Pigeonneau, F., 2020. Experimental study of bubble formation in a glass-forming liquid doped with cerium oxide. J. Am. Ceram. Soc. 103 (4), 2453–2462.

Pereira, L., et al., 2022a. A feedback mechanism between crystals and bubbles in a RuO2-bearing melt. J. Non-Cryst. Solids 582, 121456.

Pereira, L., Vasseur, J., Wadsworth, F.B., Trixler, F., Dingwell, D.B., 2022b. Interparticle and Brownian forces controlling particle aggregation and rheology of silicate melts containing platinum-group element particles. Sci. Rep. 12 (1), 9226.

Pereira, L., et al., 2023. The physics of dancing peanuts in beer. R. Soc. Open Sci. 10 (6), 230376.

Pistone, M., Cordonnier, B., Ulmer, P., Caricchi, L., 2016. Rheological flow laws for multiphase magmas: an empirical approach. J. Volcanol. Geotherm. Res. 321, 158–170.

Pistone, M., Formo, E., Whittington, A.G., Herbst, T., Cottrell, E., 2022. Direct nanoscale observations of degassing-induced crystallisation in felsic magmas. Contrib. Mineral. Petrol. 177 (3), 38.

Quemada, D., 2006. Modélisation rhéologique structurelle. Tec et Doc - Lavoisier.

Rietveld, H.M., 1969. A profile refinement method for nuclear and magnetic structures. J. Appl. Crystallogr. 2 (2), 65–71.

Russel, W.B., 1980. Review of the Role of Colloidal Forces in the Rheology of Suspensions. J. Rheol. 24 (3), 287–317.

Russell, J.K., Hess, K.-U., Dingwell, D.B., 2022. Chapter 18: Models for viscosity of geological melts. In: Daniel, R.N., Grant, S.H., Donald, B.D. (Eds.), Geological Melts.

Scarani, A., et al., 2022. A chemical threshold controls nanocrystallization and degassing behaviour in basalt magmas. Commun. Earth Environ. 3.

Schairer, J.F., Yagi, K., 1953. The system FeO-Al2O3-SiO2. J. Japan. Assoc. Mineral. Petrol. Econ. Geol. 37, 83–102.

Schuller, S., et al., 2023. Liquid-liquid phase separation in borosilicate glass enriched in MoO3 – experimental investigations and thermodynamic calculations. J. Non-Cryst. Solids 600, 121997.

Sharp, T.G., Stevenson, R.J., Dingwell, D.B., 1996. Microlites and “nanolites” in rhyolitic glass: microstructural and chemical characterization. Bull. Volcanol. 57 (8), 631–640.

Shea, T., 2017. Bubble nucleation in magmas: a dominantly heterogeneous process? J. Volcanol. Geotherm. Res. 343, 155–170.

Soldati, A., Farrell, J.A., Sant, C., Wysocki, R., Karson, J.A., 2020. The effect of bubbles on the rheology of basaltic lava flows: Insights from large-scale two-phase experiments. Earth Planet. Sci. Lett. 548, 116504.

Stickel, J.J., Powell, R.L., 2005. Fluid mechanics and rheology of dense suspensions. Annu. Rev. Fluid Mech. 37 (1), 129–149.

Thivet, S., et al., 2023. Metastable liquid immiscibility in the 2018-2021 Fani Maoré lavas: new insights for volcanic nanolite formation. Commun. Earth Environ. 4, 483.

Truby, J.M., Mueller, S.P., Llewellin, E.W., Mader, H.M., 2015. The rheology of three-phase suspensions at low bubble capillary number. Proceedings. Math. Phys. Eng. Sci. 471, 20140557–20140581.

Valdivia, P., et al., 2023. Are volcanic melts less viscous than we thought? The case of Stromboli basalt. Contrib. Mineral. Petrol. 178 (7), 45.

Vasseur, J., Wadsworth, F., Dingwell, D.B., 2023. Shear thinning and brittle failure in crystal-bearing magmas arises from local non-Newtonian effects in the melt. Earth Planet. Sci. Lett. 603, 117988–117997.

Vetere, F., Holtz, F., 2020. Rheological Behavior of partly Crystallized Silicate Melts under Variable Shear Rate. Dynam. Magma Evolut. 153–167.

Vona, A., Romano, C., Dingwell, D., Giordano, D., 2011. The rheology of crystal-bearing basaltic magmas from Stromboli and Etna. Geochim. Cosmochim. Acta 75, 3214–3236.

Wadsworth, F., et al., 2018. Combined effusive-explosive silicic volcanism straddles the multiphase viscous-to-brittle transition. Nat. Commun. 9, 1234567890.

Wilson, A.D., 1960. The micro-determination of ferrous iron in silicate minerals by a volumetric and a colorimetric method. Analyst 85 (1016), 823–827.

Yoshida, K., et al., 2023. Oxidation-induced nanolite crystallization triggered the 2021 eruption of Fukutoku-Oka-no-Ba, Japan. Sci. Rep. 13 (1), 7117.

Zandona, A., Patzig, C., Rüdinger, B., Hochrein, O., Deubener, J., 2019. TiO2(B) nanocrystals in Ti-doped lithium aluminosilicate glasses. J. Non-Crystal. Solids: X 2, 100025.

Zandonà, A., et al., 2023a. Non-stoichiometric crystal nucleation in a spodumene glass containing TiO2 as seed former: Effects on the viscosity of the residual melt. J. Non-Cryst. Solids 619, 122563.

Zandonà, A., et al., 2023b. Crystallization mechanism of gel-derived SiO2–TiO2 amorphous nanobeads elucidated by high-temperature in situ experiments. Cryst. Growth Des. 23 (6), 4545–4555.